Nano Research

ISSN 1998-0124 CN 11-5974/O4
https://doi.org/10.26599/NR.2026.94909069

Research Article

High-voltage stability of ethylene carbonate (EC) and an EC-based electrolyte for 5 V-class $LiNi_{0.5}Mn_{1.5}O_4$ batteries

Tingyu Zhao[1], Hexiang Lan[1], Jiajia Zhu[1], Weiming Wang[1], Aiping Jin[1](✉), Jun Xiong[1], Junjun Peng[1], Ming Li[2], Linghui Yu[1,3](✉)

[1] School of Chemistry and Chemical Engineering, Wuhan Textile University, 1 Sunshine Avenue, Jiangxia, Wuhan 430200, China

[2] School of Resources and Environment, Wuhan Textile University, 1 Sunshine Avenue, Jiangxia, Wuhan 430200, China

[3] Hubei Key Laboratory for Clean Recycling and Resource Utilization of Waste Fibers, Wuhan Textile University, 1 Sunshine Avenue, Jiangxia, Wuhan 430200, China

Nano Res., **Just Accepted Manuscript** • https://doi.org/10.26599/NR.2026.94909069

https://www.sciopen.com/journal/1998-0124 on Aug. 1, 2026

Just Accepted

TABLE OF CONTENTS (TOC)

Insert Table of Contents artwork here

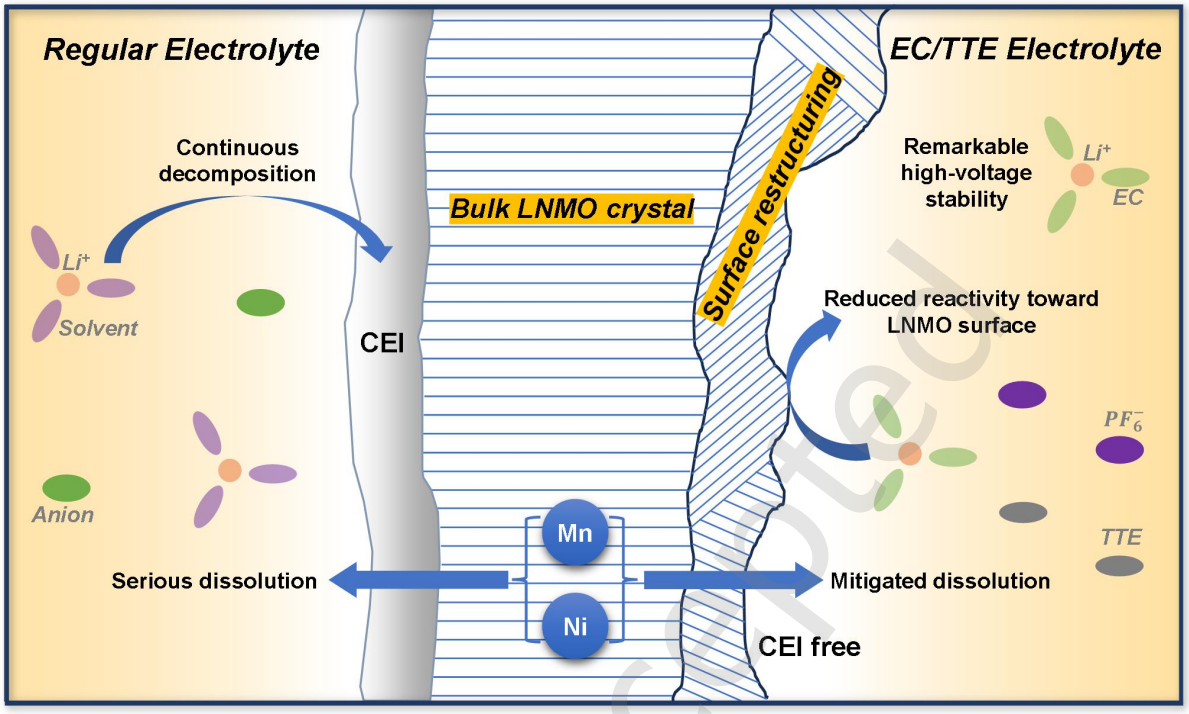

Comparison of LNMO in a regular electrolyte and the EC/TTE electrolyte

An ethylene carbonate (EC)-based electrolyte highly compatible with high-voltage $LiNi_{0.5}Mn_{1.5}O_4$ (LNMO) cathode is developed. Two insights that go against conventional understanding are uncovered, i.e. contrary to the common belief that EC decomposes readily under high voltage, it demonstrates outstanding high-voltage stability; and LNMO cycles in this electrolyte without forming a typical cathode/electrolyte interphase, experiencing instead a unique surface restructuring.

Nano Research

Open Access

Research Article

High-voltage stability of ethylene carbonate (EC) and an EC-based electrolyte for 5 V-class $LiNi_{0.5}Mn_{1.5}O_4$ batteries

Tingyu Zhao[1], Hexiang Lan[1], Jiajia Zhu[1], Weiming Wang[1], Aiping Jin[1] ✉, Jun Xiong[1], Junjun Peng[1], Ming Li[2], and Linghui Yu[1,3] ✉

[1] *School of Chemistry and Chemical Engineering, Wuhan Textile University, 1 Sunshine Avenue, Jiangxia, Wuhan 430200, China*
[2] *School of Resources and Environment, Wuhan Textile University, 1 Sunshine Avenue, Jiangxia, Wuhan 430200, China*
[3] *Hubei Key Laboratory for Clean Recycling and Resource Utilization of Waste Fibers, Wuhan Textile University, 1 Sunshine Avenue, Jiangxia, Wuhan 430200, China*

Received: 4 June 2026; **Revised:** 14 July 2026; **Accepted:** 1 August 2026

✉ Address correspondence to Aiping Jin, jinaiping2000@163.com; Linghui Yu, lhyu@wtu.edu.cn

Cite this article: *Nano Research*, 2026, 19, 94909069 https://doi.org/10.26599/NR.2026.94909069

ABSTRACT: $LiNi_{0.5}Mn_{1.5}O_4$ (LNMO) is a promising high-energy cathode material for lithium-ion batteries due to its high operating voltage (~5 V vs. Li^+/Li) which leads to a high energy density. However, the high voltage also induces unstable LNMO/electrolyte interface when cycled in regular electrolytes. In this work, we present a high-voltage ethylene carbonate (EC)/1,1,2,2-tetrafluoroethyl-2,2,3,3-tetrafluoropropylether (TTE) electrolyte that is highly compatible with $LiNi_{0.5}Mn_{1.5}O_4$ batteries. Through the use of the electrolyte, we uncover two insights that go against conventional understanding. Contrary to the common belief that EC decomposes readily under high voltage, we demonstrate the outstanding high-voltage stability of both EC and the EC/TTE electrolyte. Moreover, we find that LNMO cycles in this electrolyte without forming a typical cathode/electrolyte interphase (CEI), experiencing instead a unique surface restructuring. Under the conditions of the high-voltage stability of the electrolyte and of surface restructuring, the dissolution of nickel and manganese from LNMO is also mitigated. These features lead to long-term cyclability of LNMO batteries with an average CE of 99.86%. By challenging the perceived instability of EC and revealing a CEI-free surface restructuring process, this work offers both a practical electrolyte design and a fresh interfacial stabilization concept for high-voltage batteries.

KEYWORDS: lithium-ion battery; high-voltage; surface restructuring; cathode/electrolyte interphase; $LiNi_{0.5}Mn_{1.5}O_4$; ethylene carbonate

1 Introduction

With the urgent demand for high-energy-density energy storage devices in portable electronics and electric vehicles, high-voltage lithium-ion batteries (LIBs) have attracted much attention as a higher voltage can lead to higher energy.[1-4] In this context, spinel $LiNi_{0.5}Mn_{1.5}O_4$ (LNMO) has been considered as one of the most promising high-energy cathode materials due to its high operating voltage plateau of ~4.7 V.[5-8] However, while the high voltage offers high energy density, it also causes electrochemical oxidation of conventional electrolytes.[9, 10] This results in continuous electrolyte consumption during cycling. The resulting decomposition products may accumulate on the LNMO surface, thereby increasing cell impedance. Additionally, dissolution of nickel and manganese, often attributed to the disproportionation reaction and reactions with HF generated at high voltages, is frequently reported.[11-14] These combined effects drive rapid capacity fading of LNMO cells, presenting a major challenge to their development.[15-17]

To overcome these issues, developing a high-voltage electrolyte compatible with LNMO cathodes is crucial. Consequently, various strategies have been proposed.[18-21] For instance, high-concentration electrolytes and localized high-concentration electrolytes have been reported to be effective in improving the stability of LNMO cathodes.[22, 23] This improvement is attributed to the reduced number of free solvent molecules and the formation of an anion-derived, dense cathode/electrolyte interphase (CEI). All-fluorinated electrolytes have also shown enhanced compatibility with LNMO cathodes, as they tend to form a LiF-rich CEI.[16, 24] Sulfolane-based electrolytes are frequently employed for LNMO batteries due to the intrinsic high-voltage stability of sulfolane.[25, 26] In addition, a variety of additives, such as FEC, LiBOB, ionic additive, and silyl compounds, are being explored.[11, 27-29] These additives typically facilitate the formation of a protective CEI, which enhances electrode and electrolyte stability. Although these approaches have led to significant advances, it remains a great challenge to develop a high-voltage electrolyte for LNMO batteries with long-term stability.

In this work, we employ EC as the sole solvent, with 1,1,2,2-tetrafluoroethyl-2,2,3,3-tetrafluoropropylether (TTE) as a diluent, to formulate a high-voltage EC/TTE electrolyte that is highly compatible for LNMO batteries. We first demonstrate the exceptional high-voltage stability of EC and the EC/TTE electrolyte. This is contrary to the conventional view because EC is generally considered unstable at high voltages.[30-35] We subsequently find that LNMO remains CEI-free and undergoes surface restructuring during cycling in the EC/TTE electrolyte, a behavior that is distinctly different from that observed with traditional electrolytes. The restructuring reduces the reactivity of the surface towards electrolyte decomposition. The dissolution of nickel and manganese is also mitigated in the electrolyte. With the high-voltage stability of the electrolyte, the reduced surface reactivity, and the mitigated metal dissolution, LNMO batteries achieve remarkable cycling stability. The differences between LNMO in a regular electrolyte and LNMO in the EC/TTE electrolyte are summarized in **Figure 1**.

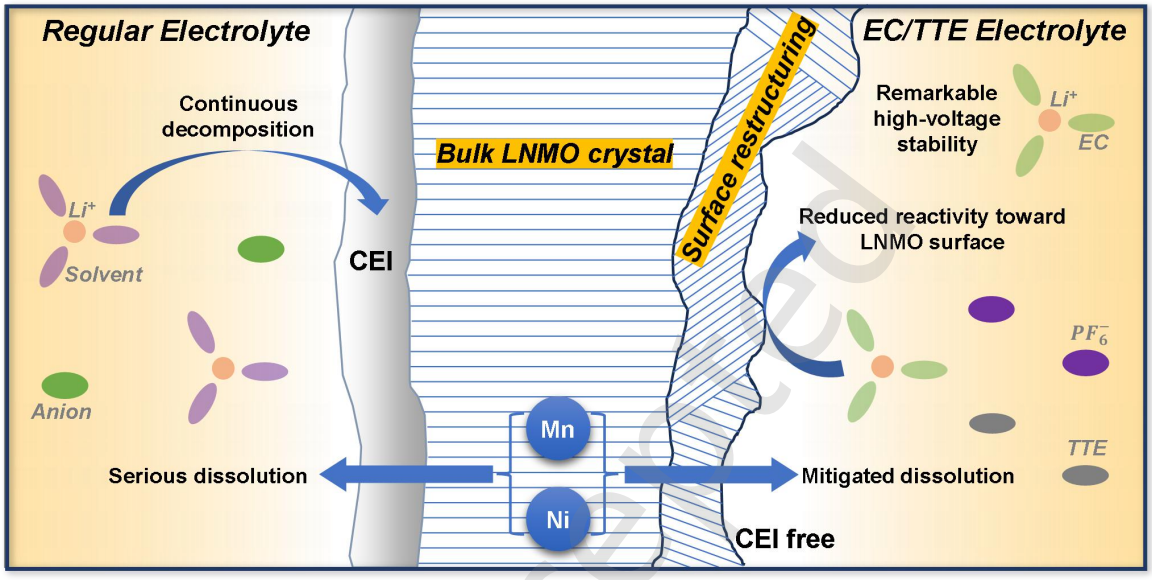

Figure 1. Comparison of LNMO in a regular electrolyte and the EC/TTE electrolyte

2 Results and discussion

EC was employed as the sole solvent to dissolve $LiPF_6$ in this study. To lower the high melting point of EC, 1,1,2,2-tetrafluoroethyl-2,2,3,3-tetrafluoropropylether (TTE), a widely used non-solvent diluent,[30, 36-39] was introduced, forming an EC/TTE electrolyte (0.5 M $LiPF_6$ in EC/TTE, 1/1 by volume). For comparison, a control electrolyte was made by adding TTE to a commercial electrolyte (LB-240, 1 M $LiPF_6$ in DEC/EC/EMC (1/1/1 by volume) with 1 wt% vinylene carbonate (VC)), yielding LB-240/TTE (1/1 by volume, 0.5 M $LiPF_6$). Because TTE is a non-solvent diluent, its addition does not change the solvation structure of the electrolytes, which is confirmed by Raman spectroscopy (**Figure S1**).

The electrochemical oxidation stability of the two electrolytes was first evaluated. **Figure 2**a shows linear sweep voltammetry (LSV) tests of Li/Al cells at a scanning rate of 5 mV s^{-1}. It seems that the onset oxidation voltage is ~4 V vs. Li^+/Li. This is rather low and consistent with literature.[40]. However, at 6 V vs. Li^+/Li, the current densities for both electrolytes are lower than 0.04 mA cm^{-2}. This is much lower than many high-voltage electrolytes reported,[25, 29, 41-45] indicating that both electrolytes possess high resistance to electrochemical oxidation at high voltages. The current in the voltage range below 4.6 V is mainly attributed to the formation of a passivation layer on the aluminum.[46, 47]

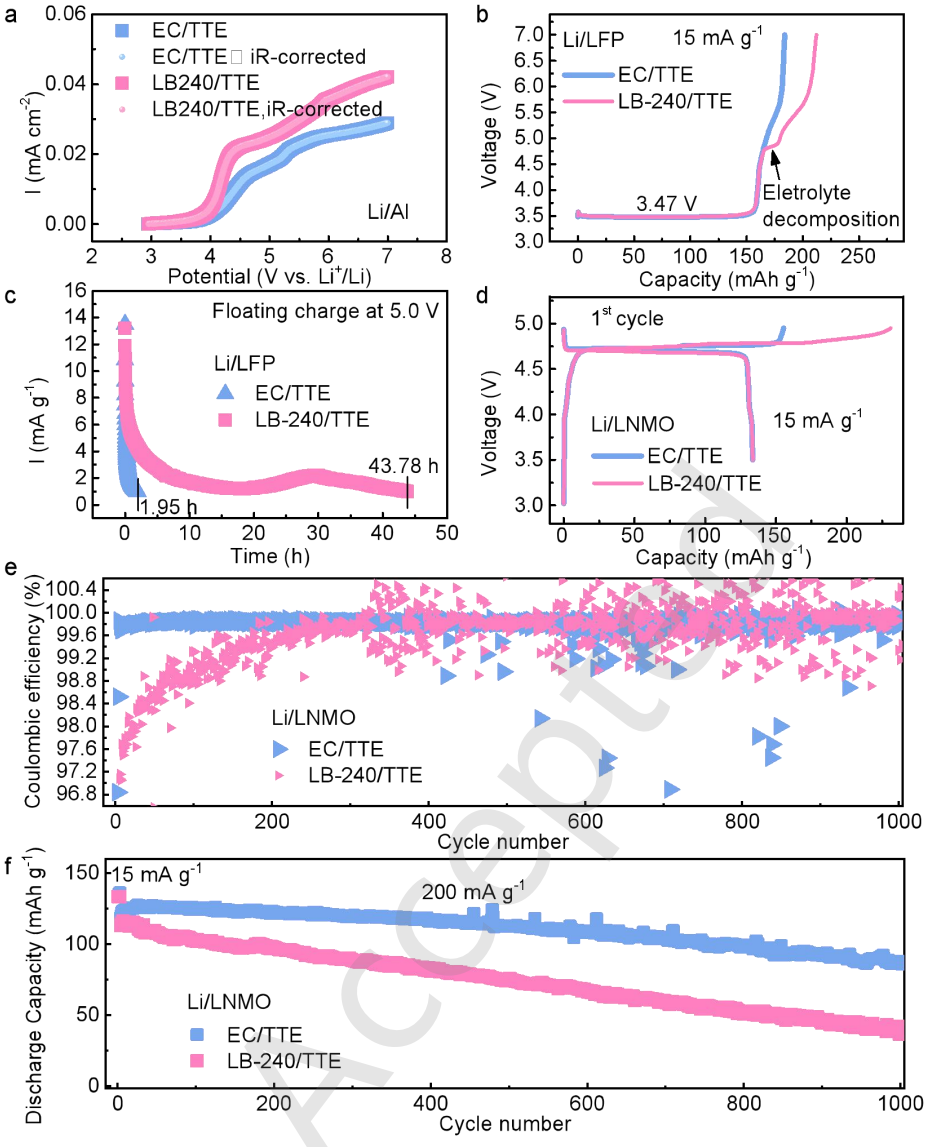

Figure 2. Electrochemical properties of Li/Al, Li/LFP, and Li/LNMO cells. (a) LSV of Li/Al cells. Scanning rate: 5 mV s^{-1}. The Nyquist plots of the cells used for the iR correction are shown in **Figure S2**; (b) the first-charge voltage profiles of Li/LFP cells; (c) floating charge tests Li/LFP cells at 5 V. Before the potentiostatic process, the cells were first galvanostatically charged to 5 V at a 15 mA g^{-1}; (d) the first charge/discharge profiles of Li/LNMO cells; (e) CEs of Li/LNMO cells; (f) cyclability of Li/LNMO cells.

To better evaluate the electrochemical oxidation stability, we tested the high-voltage behaviors of Li/LFP cells with the two electrolytes (Figure 2b). The LFP electrode contains aluminum current collector, conductive carbon and high-voltage stable LFP, giving more conditions for surface-effect examinations at high voltages. Moreover, compared to Li/Al cell, Li/LFP cell has a flat charging voltage plateau at ~3.47 V, providing an ideal reference for comparison. This plateau corresponds to the electrochemical oxidation of LFP. In addition to this plateau, there is another electrochemical oxidation plateau at ~4.85 V observed for the cell with LB-240/TTE. This plateau is related to electrolyte decomposition. In contrast, the cell with the EC/TTE electrolyte has no additional electrolyte decomposition plateau in the voltage range from 4 V to 7 V. This demonstrates the remarkable stability of the EC/TTE electrolyte at high voltages. We also performed floating charge tests of Li/LFP cells at 5 V (Figure 2c). The current reduces to 1 mA g^{-1} in 1.95 h for the cell with the EC/TTE electrolyte, whereas it takes 43.78 h to reduce to the same current density for the cell with LB-240/TTE. This further confirms the excellent stability of the EC/TTE electrolyte at 5 V vs. Li^+/Li.

The Li/Al and Li/LFP cells indicate that the EC/TTE electrolyte possesses remarkable high-voltage stability. As abundant EC molecules in the electrolyte remain uncoordinated (Figure S1), these results also indicate that EC is highly stable at high voltages. This suggests that EC is a promising solvent for high-voltage electrolytes, which challenges the commonly held belief that EC is unsuitable for high-voltage applications.

Figure 2d shows the first charge/discharge voltage profiles of Li/LNMO cells at a current density of 15 mA g^{-1}. More voltage profiles at 15 mA g^{-1} and 200 mA g^{-1} can be found in **Figure S3** for comparison. The initial charge capacity for the

LB-240/TTE cell is 230.9 mAh g^{-1}, far larger than the theoretical capacity of LNMO (146.7 mAh g^{-1}), indicating serious electrolyte decomposition due to the high voltage plateaus (4.7 V – 4.8 V) and the high cut-off voltage (4.95 V). The first charge capacity of the EC/TTE cell is 155.3 mAh g^{-1}, also exceeding the theoretical value and indicating decomposition of the electrolyte. The discharge voltage profiles for the two electrolytes are nearly identical, resulting in the same discharge capacity of 133.4 mAh g^{-1}. The corresponding initial Coulombic efficiency (CE) for the LB-240 cell is 57.8 %. This is much lower than that (85.9 %) for the EC/TTE cell. The low CE is attributed to the poor reversibility of electrolyte decomposition, which reduces the overall reversibility of the cell reactions. The CE increases continuously during the following cycles (**Figure S4**). This suggests that a protective layer that prevents electrolyte decomposition form on the LNMO electrode upon cycling.

The CE of the EC/TTE cell is generally larger than 99.8 % over 1000 cycles at 200 mA g^{-1} (Figure 2e). The high CE indicates the electrochemical inactivity of the electrolyte on the LNMO surface. In contrast, it takes more than 200 cycles for the CE of the LB-240/TTE cell to increase from 95 % to ~99.7 % at 200 mA g^{-1} (Figure 2e and Figure S4). This lower CE of the LB-240/TTE cell than that of the EC/TTE cell indicates that the LB-240/TTE electrolyte decomposes more seriously on the LNMO electrode during cycling. The CE of the EC/TTE cell drops to low values on certain cycles between 400 and 900 (Figure S4). We believe this is not caused by irreversible electrolyte decomposition on the cathode, but by internal short circuits due to lithium dendrite growth, as evidenced by the noisy charging voltage profile. An example is shown in **Figure S5**.

Figure 2f shows the cyclability of Li/LNMO cells with the two electrolytes. The EC/TTE cell has a discharge capacity of 118.5 mAh g^{-1} at cycle 4 at 200 mA g^{-1}. After 1000 cycles at the same current density, the cell retains a discharge capacity of 86.7 mAh g^{-1} (cycle 1003), corresponding to a capacity retention of 73.2 %. By comparison, the LB-240/TTE cell only maintains a retention of 34.1 %.

The long cyclability of the EC/TTE cell is partially attributed to the high-voltage stability of the EC/TTE electrolyte as demonstrated above. Besides, the reactivity of electrolyte toward LNMO surface is also crucial for the cycling performance because of surface interactions. To evaluate the reactivity, density functional theory (DFT) calculations were performed on the fully delithiated LNMO ($Ni_{0.5}Mn_{1.5}O_4$) material. H transfer can occur for all solvents and TTE used in the two electrolytes, which means that all solvents and TTE tend to react with the $Ni_{0.5}Mn_{1.5}O_4$ surface **(Figure 3** and **Figure S6)**. For each solvent/diluent, the highest reaction energy decreases in the order of EC (-1.85 eV) > VC (-1.34 eV) > DEC (-0.82 eV) > EMC (-0.34 eV) > TTE (-0.25 eV). This suggests that EC is the most reactive. This is not consistent with stable cyclability and high CE using the EC/TTE electrolyte.

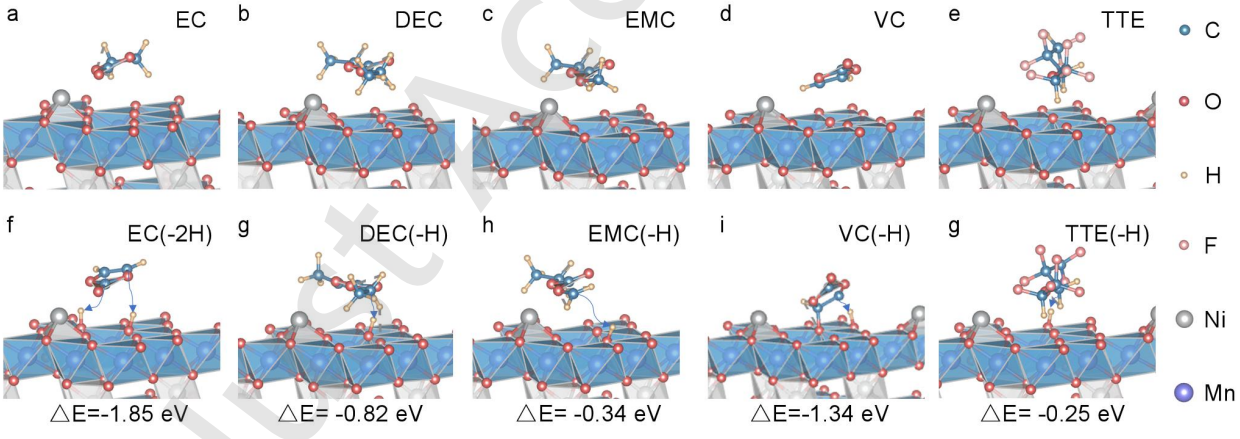

Figure 3. Reactivity of EC, DEC, EMC, VC, and TTE at the fully charged delithiated LNMO ($Ni_{0.5}Mn_{1.5}O_4$) surface (Fd3m, (111)) from DFT+U calculations. (a-e) Initial configurations; and (f-g) final configurations with the highest reaction energies of each molecular. More calculation results can be found in Figure S6. Arrows indicate H transfer reaction from solvent to surface oxygen. H transfer occurring at different positions gives different reaction energies. *ΔE*, the energy difference between the physisorbed solvent molecule and the reacted solvent/TTE

To gain more insight into the electrolyte reactivity, XPS was conducted on the LNMO electrodes charged to 4.95 V vs. Li^+/Li (**Figure 4**). For comparison, we also performed XPS analysis on pristine LNMO and a fresh LNMO electrode (**Figure S7**). The C 1s spectra show the presence of C-C, C-O, C=O, O-C=O, and CF_2/ CO_3^{2+} for both electrodes cycled in the two electrolytes (Figures 4a and d). However, compared to the electrode in the EC/TTE electrolyte, the one in the LB-240/TTE electrolyte shows a much more pronounced peak for oxygen-containing species (C-O, C=O, O-C=O, and CF_2/ CO_3^{2+}), along with higher relative contents of these species (**Figure S8** and **Table S1**). This confirms that the decomposition of carbonate solvents is much more serious in the LB-240/TTE electrolyte than in the EC/TTE electrolyte during cycling.

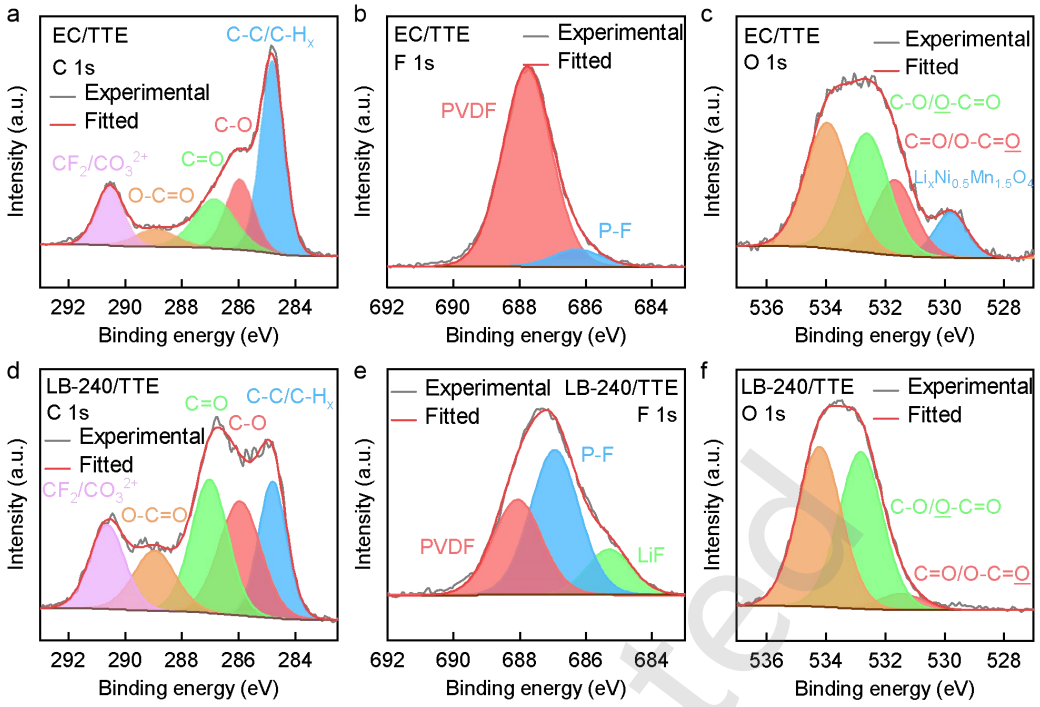

Figure 4. XPS spectra of LNMO charged to 4.95 V vs. Li^+/Li (10^{th} charge). C 1s (a), F 1s (a), and O 1s (a) spectra in the EC/TTE electrolyte; C 1s (d), F 1s (e), and O 1s (f) spectra in the LB-240/TTE electrolyte

The F 1s spectra (Figures 4b and e) shows a dominant C- F peak with a minor P- F peak for the electrode in EC/TTE electrolyte. By contrast, the electrode in LB-240/TTE electrolyte exhibits a stronger P- F peak than the C- F peak, as well as a LiF peak. The C- F signal comes from the PVDF binder, whereas the P- F species and LiF are decomposition products of $LiPF_6$. These results suggest that $LiPF_6$ undergoes more severe decomposition in LB-240/TTE electrolyte compared to EC/TTE electrolyte during cycling.

In the O 1s spectra (Figures 4c and f), an oxide (delithiated LNMO) peak is present for the electrode cycled in the EC/TTE electrolyte but absent for that cycled in the LB-240/TTE electrolyte. This absence is because the LNMO particles in the LB-240/TTE electrolyte are covered by a thick CEI layer, as will be discussed later.

The XPS results above demonstrate that the LB-240/TTE electrolyte is more reactive toward the LNMO surface than the EC/TTE electrolyte during cycling. This is consistent with the electrochemical results.

To further understand the electrolyte reactivity on the LNMO surface, transmission electron microscopy (TEM) analysis was performed on the LNMO materials charged to 4.95 V vs. Li^+/Li (10^{th} charge). **Figure 5**a shows the TEM image of the LNMO cycled in the LB-240/TTE electrolyte. The formation of CEI is evidenced by the presence of an amorphous phase on the surface. The core of the particle maintains a single-crystal structure (Figures 5a and b), consistent with the pristine LNMO particle (**Figure S9**). In contrast, the LNMO particle cycled in the EC/TTE electrolyte exhibits anomalous characteristics distinctly different from those observed with traditional electrolytes.[48-50] It lacks an amorphous CEI layer on the surface (Figures 5c, d, and **Figure S10**), suggesting that EC is not conducive to CEI formation. Moreover, the surface regions exhibit crystal plane orientations distinct from the bulk (Figure 5d and Figure S10). Furthermore, the diffraction spots of the SAED pattern are elongated, indicating the presence of defects (Figure 5e). The structural inhomogeneity of the LNMO cycled in the EC/TTE electrolyte contrasts with the pristine LNMO and the LNMO cycled in the LB-240/TTE electrolyte. These results indicate that the CEI layer protects the crystal structure during cycling. Conversely, without the CEI layer, the particle surface undergoes restructuring. Combining the electrochemistry, DFT, XPS, and TEM studies, it is concluded that the surface restructuring reduces the reactivity of the surface toward electrolyte decomposition. In contrast, the CEI layer formed in the LB-240/TTE electrolyte is less effective in protecting the electrolyte from decomposition.

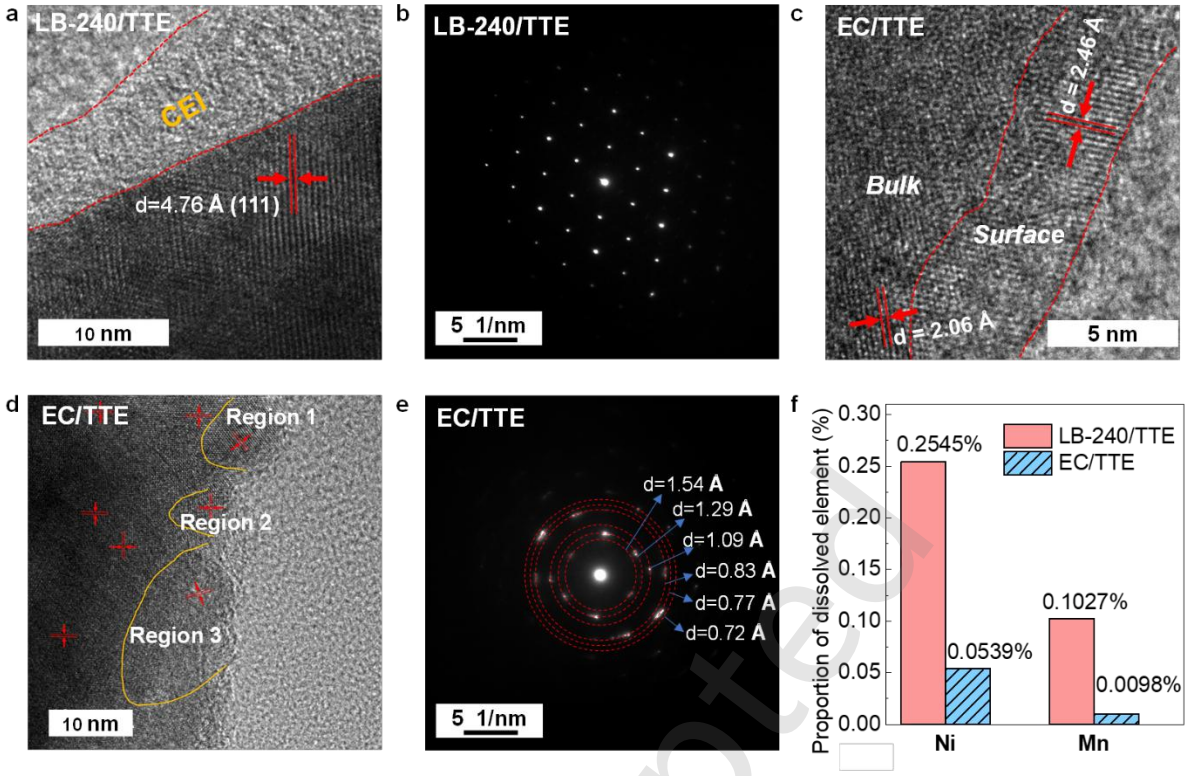

Figure 5. TEM and ICP analysis. (a – e) TEM images and SAED patterns of LNMO charged to 4.95 V vs. Li^+/Li. (a and b) Cycled in the LB-240/TTE electrolyte; (c – e) cycled in the EC/TTE electrolyte. (f) Nickel and Manganese dissolution percentages after 103 cycles, each normalized to the respective metal content in LNMO and determined by ICP.

It is often reported that the nickel and manganese in LNMO dissolve into the electrolyte during cycling. To investigate their dissolution in the electrolyte, inductively coupled plasma optical emission spectrometry (ICP-OES) measurements were performed on the electrolytes collected from Li/LNMO cells after 103 cycles. The results are shown in Figure 5f. The proportions of dissolved nickel and manganese are 0.25% and 0.10%, respectively, for the LNMO cycled in the LB-240/TTE electrolyte, and 0.05% and 0.01% for that cycled in the EC/TTE electrolyte. The limited dissolution of nickel and manganese in the EC/TTE electrolyte is possibly due to the high-voltage stability of the electrolyte. This stability minimizes HF generation by suppressing the oxidative dehydrogenation of the carbonate solvent and thus mitigating nickel and manganese dissolution.[31, 51] Additionally, surface restructuring may further inhibit metal dissolution.

Based on the studies above, we summarize the advantages of the EC/TTE electrolyte for high-voltage LNMO cathodes (Figure 1). Firstly, the electrolyte is remarkably stable at high voltages. Secondly, LNMO undergoes surface restructuring in the EC/TTE electrolyte during cycling, which reduces the reactivity of the electrolyte toward the LNMO surface. Thirdly, in the EC/TTE electrolyte, the dissolution of nickel and manganese ions is mitigated during cycling. With these advantages, LNMO exhibits excellent cyclability in the EC/TTE electrolyte.

To further examine the electrochemical properties of the two electrolytes, Gr/LNMO full cells were tested. The full cells with the two electrolytes have similar polarization and capacities during the initial three cycles at 15 mA g^{-1} (**Figure 6**a). The current density and capacity of full cells were calculated based on the mass of LNMO. From the 4th cycle, the cells were cycled at 100 mA g^{-1}. At the 10th cycle, the LB-240/TTE cell exhibits greater polarization than the other cell, due to more serious degradation. The EC/TTE cell exhibits long cyclability. It delivers a capacity of 111.8 mAh g^{-1} at the 4th cycle, and a capacity of 73.5 mAh g^{-1} remains after 500 cycles at 100 mA g^{-1}, corresponding to a capacity retention of 66%. In comparison, after only ~200 cycles under the same current density, the capacity of the LB-240/TTE cell drops to ~10 mAh g^{-1} and can not be recovered at a reduced current density of 15 mA g^{-1} (Figure 6b). The EC/TTE cell also exhibits high CE (Figure 6c). The initial CE is 87.6%. It increases to above 99.5 % within a few cycles and stabilizes at ~99.9%. The average CE from the 4th to the 503rd cycle is 99.86%, calculated by dividing the sum of discharge capacities by the sum of the charge capacities. By contrast, the CE of the LB-240/TTE cell is much lower, with an initial value of 79.6% and primarily remaining between 95% and 99%.

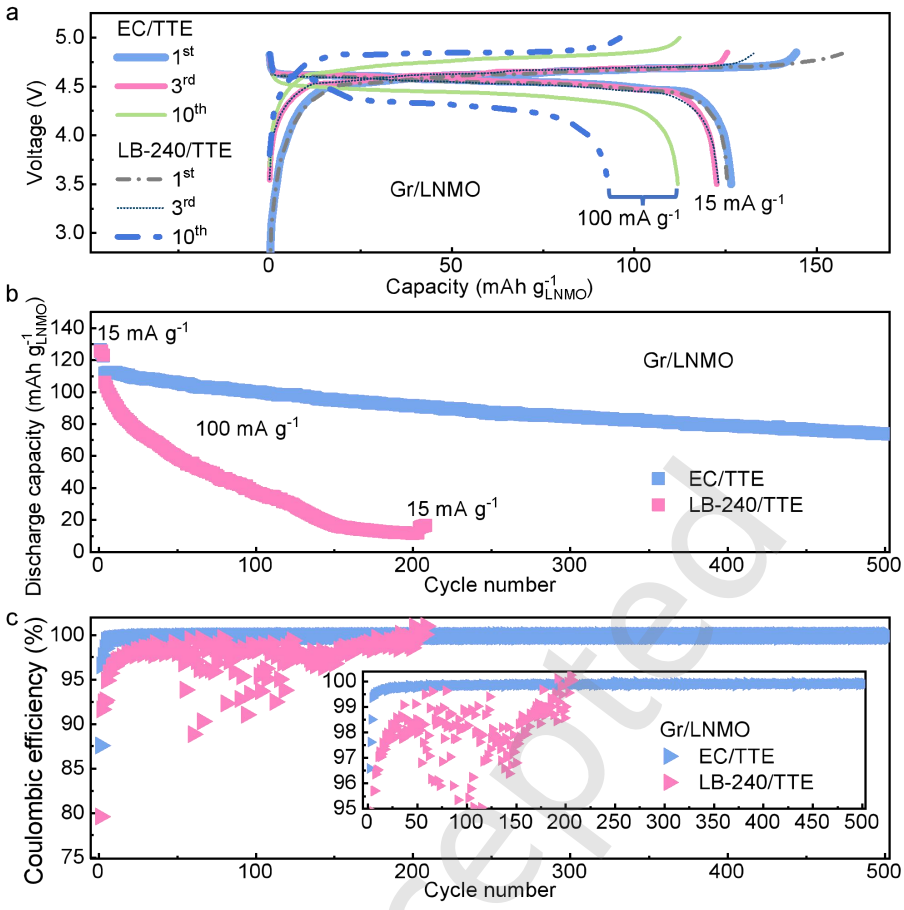

Figure 6. Properties of Gr/LNMO full cells. (a) Charge/discharge profiles; (b) cyclability; and (c) CEs, inset showing an enlarged region

The difference in stability between the two full cells is mainly attributable to the varying stability of the cathode (LNMO) sides that are discussed above. This is because the Gr anode in the two electrolytes show negligible differences (**Figure S11**). It needs to be noted that, in the LB-240/TTE electrolyte, the mismatch between the CEs of the LNMO cathode (mostly below 99% in the initial 100 cycles, Figure 2e) and the Gr anode (stable at ~99.7% after a few cycles, Figure S11c) contributes to the rapid degradation of the corresponding full cell.

In addition to the high-voltage stability, the EC/TTE electrolyte also gives enhanced safety as it is non-flammable, whereas the LB-240/TTE electrolyte is highly flammable like conventional organic electrolytes (**Figure S12**).

3 Conclusions

In this work, we develop a high-voltage EC/TTE electrolyte highly comparable with LNMO batteries. We first demonstrated the exceptional high-voltage stability of EC and an EC/TTE electrolyte on Al and LFP electrodes. This challenges the common belief that EC is unstable under high voltage. We subsequently found that LNMO remained CEI-free and undergoes surface restructuring during cycling in the EC/TTE electrolyte, a behavior that is distinctly different from that observed with traditional electrolytes. The restructuring is attributed to the absence of CEI as the presence of CEI helped protect the crystal structure. A combination of electrochemistry, DFT, XPS, and TEM studies confirmed that this restructuring reduced the reactivity of the LNMO surface toward electrolyte decomposition. Moreover, the dissolution of nickel and manganese from LNMO was also mitigated under the conditions of the high-voltage stability of the electrolyte and of surface restructuring. With the high-voltage stability of the electrolyte, the reduced surface reactivity, and the mitigated metal dissolution, LNMO cathode retained 73.2% of capacity over 1000 cycles at 200 mA g^{-1}. High-voltage Gr/LNMO full cell also demonstrated long-term cyclability, maintaining 66% capacity retention over 500 cycles at 100 mA g^{-1} with an average CE of 99.86%. The demonstration of the exceptional high-voltage stability of EC offers a viable strategy for the development of high-voltage batteries. The surface restructuring observed provides an effective approach to enhance the stability of both the LNMO cathode and the electrolyte.

Electronic Supplementary Material: Supplementary material (experimental section, Raman spectra, Charge/discharge voltage profiles of Li/LNMO cells, Nyquist plots, Full range CEs of Li/LNMO, Example of a shorting voltage profile, Additional DFT calculation results, Additional XPS results, Additional TEM results, Additional properties of Li/Gr cells, Flammability tests) is available in the online version of this article at https://doi.org/10.26599/NR.2026.94909069.

Data availability

All data needed to support the conclusions in the paper are presented in the manuscript and/or the Electronic Supplementary Material. Additional data related to this paper may be requested from the corresponding author upon request.

Acknowledgements

This work was supported by the National Natural Science Foundation of China (No. 52577234) and the Wuhan Textile University Fund B (k24098 and K25025). Authors thank the Analytical and Testing Center at Wuhan Textile University for materials characterizations.

Declaration of competing interest

All the contributing authors report no conflict of interests in this work.

Author contribution statement

T.Z.: Validation, Investigation, Data Curation, Writing - Original Draft, Visualization. **H.L.:** Investigation. **J.Z.:** Investigation. **W.W.:** Writing - Review & Editing. **A.J.:** Resources, Supervision, Writing - Review & Editing. **J.X.:** Writing - Review & Editing. **J.P.:** Funding acquisition, Writing - Review & Editing. **M.L.:** Resources**,** Writing - Review & Editing. **L.Y.:** Conceptualization, Visualization, Supervision, Funding acquisition, Writing - Review & Editing.

Use of AI statement

None.

References

[1] Zhang, A.;Bi, Z.;Yang, E.;Chen, T.;Li, X.;Liao, S.;Wang, G.;Yu, Y.;Bao, X.; Wu, Z.-S. Formulating Electrophilic Electrolyte for In Situ Stabilization of 4.8 V Li-Rich Batteries with 100% Initial Coulombic Efficiency. *Angew. Chem. Int. Ed.* **2025**, *64*, e202502603.

[2] Liu, Y.;Sun, Y.;Jiang, S.;Li, S.;Qu, C.;Deng, D.;Zou, B.;Hou, Q.;Feng, X.;Wang, J.; Xiang, H. In situ homogenized fluorination strategy via active prelithiation enabling LiF solid electrolyte interphases for stable silicon anodes. *Energy Environ. Sci.* **2025**, *18*, 10216–10227.

[3] Guo, Y.;Jie, Y.;Zhang, Z.;Yi, Y.;Wang, Y.;Dong, Y.;Wang, K.;Liu, Y.;Lei, Z.;Cheng, T.;Cao, R.;Yu, Y.; Jiao, S. Enabling 5V-class lithium metal batteries via an aggregation-enhanced solvation electrolyte. *Nano Research* **2026**, 10.26599/NR.2026.94908856.

[4] Zhang, S.;Zhu, H.;Hua, J.;Wang, J.;Li, L.;Chen, L.;Li, R.;Chen, L.;Fan, X.; Deng, T. Dielectric-mediated interfacial ion transport enabling stable lithium metal batteries. *Carbon Future* **2026**, *3*, 9200068.

[5] Jobst, N. M.;Paul, N.;Beran, P.;Mancini, M.;Gilles, R.;Wohlfahrt-Mehrens, M.; Axmann, P. Dynamic Structure Evolution of Extensively Delithiated High Voltage Spinel Li1+xNi0.5Mn1.5O4 x < 1.5. *J. Am. Chem. Soc.* **2023**, *145*, 4450-4461.

[6] Shin, H.;Ndukwe, A.;Kim, T.;Lee, J. H.;Li, G. C.; Lee, H. J. Mitigating Diffusion-Induced Intragranular Cracking in Single-Crystal LiNi0.5Mn1.5O4 via Extended Solid-Solution Behavior. *Angew. Chem. Int. Ed.* **2025**, *64*, e202422726.

[7] Liao, Q.-T.;Sun, Y.-G.;Guo, S.-J.;Wang, J.;Wu, T.-T.;Cao, A.-M.; Wan, L.-J. Construction of metal phosphate coatings for improved performance of high-voltage cathode. *Nano Research* **2025**, *18*, 94907831.

[8] Stüble, P.;Mereacre, V.;Geßwein, H.; Binder, J. R. On the Composition of LiNi0.5Mn1.5O4 Cathode Active Materials. *Adv. Energy Mater.* **2023**, *13*, 2203778.

[9] Song, J.;Shin, D. W.;Lu, Y.;Amos, C. D.;Manthiram, A.; Goodenough, J. B. Role of Oxygen Vacancies on the Performance of Li[Ni0.5−xMn1.5+x]O4 (x = 0, 0.05, and 0.08) Spinel Cathodes for Lithium-Ion Batteries. *Chem. Mater.* **2012**, *24*, 3101-3109.

[10] Nisar, U.;Klein, F.;Pfeifer, C.;Wohlfahrt-Mehrens, M.;Hölzle, M.; Axmann, P. Elucidating the nature of secondary phases in LiNi0.5Mn1.5O4 cathode materials using correlative Raman-SEM microscopy. *Energy Storage Materials* **2025**, *74*, 103905.

[11] Wang, B.;Doan, H. A.;Son, S.-B.;Abraham, D. P.;Trask, S. E.;Jansen, A.;Xu, K.; Liao, C. Data-driven design of electrolyte additives supporting high-performance 5 V LiNi0.5Mn1.5O4 positive electrodes. *Nat. Commun.* **2025**, *16*, 3413.

[12] Wu, L.;Wang, S.;Niu, Y.;Sun, Z.;Yao, X.; Xu, Y. High-rate LiNi0.5Mn1.5O4 cathode materials for Li-ion batteries by the strategy of multi-ion co-doping. *Chem. Eng. J.* **2025**, *516*, 163892.

[13] Seok, E.;Kim, M.;Lee, S.;Park, J.;Ku, M.;Lim, H.;Lee, Y.;Yu, S.; Choi, W. Electrostatic interaction-driven inorganic coating layer toward improving battery performance for 5 V class high-voltage cathode in secondary batteries. *Chem. Eng. J.* **2023**, *453*, 139737.

[14] Zhu, X.;Schülli, T. U.;Yang, X.;Lin, T.;Hu, Y.;Cheng, N.;Fujii, H.;Ozawa, K.;Cowie, B.;Gu, Q.;Zhou, S.;Cheng, Z.;Du, Y.; Wang, L. Epitaxial growth of an atom-thin layer on a LiNi0.5Mn1.5O4 cathode for stable Li-ion battery cycling. *Nat. Commun.* **2022**, *13*, 1565.

[15] Dou, Y.;Zhou, S. Y.;Dawkins, J. I. G.;Zaghib, K.;Amine, K.;Xu, G. L.; Deng, S. X. Manganese-Based Spinel Cathodes: A Promising Frontier for Solid-State Lithium-Ion Batteries. *Adv. Mater.* **2025**, *38*, e14126.

[16] Suo, L.;Xue, W.;Gobet, M.;Greenbaum, S. G.;Wang, C.;Chen, Y.;Yang, W.;Li, Y.; Li, J. Fluorine-donating electrolytes enable highly reversible 5-V-class Li metal batteries. *Proceedings of the National Academy of Sciences* **2018**, *115*, 1156-1161.

[17] Murdock, B. E.;Cen, J.;Squires, A. G.;Kavanagh, S. R.;Scanlon, D. O.;Zhang, L.; Tapia-Ruiz, N. Li-Site Defects Induce Formation of Li-Rich Impurity Phases: Implications for Charge Distribution and Performance of LiNi0.5−xMxMn1.5O4 Cathodes (M = Fe and Mg; x = 0.05–0.2). *Adv. Mater.* **2024**, *36*, 2400343.

[18] Yue, H.;Yang, Y.;Xiao, Y.;Dong, Z.;Cheng, S.;Yin, Y.;Ling, C.;Yang, W.;Yu, Y.; Yang, S. Boron additive passivated carbonate electrolytes for stable cycling of 5 V lithium–metal batteries. *J. Mater. Chem. A* **2019**, *7*, 594-602.

[19] Sun, J.;Kang, S.;Wu, X.;Lou, X.;Shen, M.; Hu, B. Biphasic synergistic functional electrolyte enhances high-temperature performance of 4.85 V LiNi0.5Mn1.5O4||graphite pouch cells. *Energy Storage Materials* **2026**, *86*, 104950.

[20] Zhong, H.;Lu, J.;He, A.;Sun, M.;He, J.; Zhang, L. Carboxymethyl chitosan/poly(ethylene oxide) water soluble binder : Challenging application for 5V LiNi0.5Mn1.5O4 cathode. *Journal of Materials Science & Technology* **2017**, *33*, 763-767.

[21] He, R.;Zhang, T.;Liu, F.;Li, J.;Wu, J.;Xiao, X.;Wu, X.;Wang, J.;Li, Y.;Pan, F.;Deng, Y.; Zhang, G. Moderate Solvation Structure Design Endows Long Cycling of 5 V-Class Fast-Charging Lithium-Ion Batteries. *ACS Energy Letters* **2026**, *11*, 1993-2004.

[22] Guan, D.;Zeng, J.;Xue, Z.;Cao, Y.;Hu, G.;Peng, Z.; Du, K. Rational Design of the Li+-Solvation Structure Contributes to Constructing a Robust Cathode-Electrolyte Interphase for a 5 V High-Voltage LiNi0.5Mn1.5O4 Cathode. *ACS Applied Energy Materials* **2023**, *6*, 9568-9576.

[23] Zhang, J.;Cohen, O.;Lang, X.;Wang, B.;Trask, S. E.;Cho, K.;Persson, K. A.; Su, L. Delineating the Impact of Diluent on High-Concentration Electrolytes for Developing High-Voltage LiNi0.5Mn1.5O4 Spinel Cathode. *Small* **2025**, *21*, 2502141.

[24] Hu, L.;Zhang, Z.; Amine, K. Fluorinated electrolytes for Li-ion battery: An FEC-based electrolyte for high voltage LiNi0.5Mn1.5O4/graphite couple. *Electrochem. Commun.* **2013**, *35*, 76-79.

[25] Hai, F.;Tian, X.;Yi, Y.;Wu, Z.;Zheng, S.;Guo, J.;Tang, W.;Hua, W.; Li, M. A sulfolane-based high-voltage electrolyte with dispersed aggregates for 5 V batteries. *Energy Storage Materials* **2023**, *54*, 641-650.

[26] Lu, D.;Xu, G.;Hu, Z.;Cui, Z.;Wang, X.;Li, J.;Huang, L.;Du, X.;Wang, Y.;Ma, J.;Lu, X.;Lin, H.-J.;Chen, C.-T.;Nugroho, A. A.;Tjeng, L. H.; Cui, G. Deciphering the Interface of a High-Voltage (5 V-Class) Li-Ion Battery Containing Additive-Assisted Sulfolane-Based Electrolyte. *Small Methods* **2019**, *3*, 1900546.

[27] Li, L.;Yang, T.;Ren, K.;Song, X.;Wu, S.;Li, H.-W.;Jiang, Z.;Sun, M.; Li, Y. Silyl additives-driven synergistic inhibition engineering enables 4.9 V LiNi0.5Mn1.5O4 batteries beyond 300 Wh kg−1. *Materials Today* **2025**, *90*, 249-257.

[28] Huang, L.;Xiao, X.;Ding, G.;Li, W.;Fang, W.;Xia, H.-l.;Cheng, T.;Zang, X.-F.;He, L.; Kong, L. Engineering interfacial chemistry and solvation structure via a novel ionic additive for ~ 5 V-class LiNi0.5Mn1.5O4 batteries. *J. Colloid Interface Sci.* **2026**, *707*, 139742.

[29] Li, T.;Chen, Z.;Bai, F.;Li, C.; Li, Y. Diluted low concentration electrolyte for interphase stabilization of high-voltage LiNi0.5Mn1.5O4 cathode. *Journal of Energy Chemistry* **2023**, *81*, 404-409.

[30] Yang, Q.;Lv, X.;Fu, Y.;Xu, K.; Guo, W. Ligand exchange of Li-ion solvation sheath enables balanced electrolytes. *Joule* **2025**, *9*, 101821.

[31] Zhou, T.;Chen, L.;Zhang, H.;Li, R.;Zhang, S.;Ma, B.;Wang, J.;Huang, J.;Zhu, H.;Hua, J.;Liu, Z.;Zhang, H.;Wang, K.;Chen, L.;Deng, T.; Fan, X. Tuning interfacial solvent orientation for high-voltage lithium-ion batteries. *Chem* **2025**, *12*, 102819.

[32] Fan, X.;Chen, L.;Borodin, O.;Ji, X.;Chen, J.;Hou, S.;Deng, T.;Zheng, J.;Yang, C.;Liou, S.-C.;Amine, K.;Xu, K.; Wang, C. Non-flammable electrolyte enables Li-metal batteries with aggressive cathode chemistries. *Nat. Nanotechnol.* **2018**, *13*, 715-722.

[33] Peljo, P.; Girault, H. H. Electrochemical potential window of battery electrolytes: the HOMO–LUMO misconception. *Energy Environ. Sci.* **2018**, *11*, 2306-2309.

[34] Zhang, X.;Pugh, J. K.; Ross, P. N. Computation of Thermodynamic Oxidation Potentials of Organic Solvents Using Density Functional Theory. *J. Electrochem. Soc.* **2001**, *148*, E183.

[35] Giordano, L.;Karayaylali, P.;Yu, Y.;Katayama, Y.;Maglia, F.;Lux, S.; Shao-Horn, Y. Chemical Reactivity Descriptor for the Oxide-Electrolyte Interface in Li-Ion Batteries. *The Journal of Physical Chemistry Letters* **2017**, *8*, 3881-3887.

[36] Xu, J.;Zhang, J.;Pollard, T. P.;Li, Q.;Tan, S.;Hou, S.;Wan, H.;Chen, F.;He, H.;Hu, E.;Xu, K.;Yang, X.-Q.;Borodin, O.; Wang, C. Electrolyte design for Li-ion batteries under extreme operating conditions. *Nature* **2023**, *614*, 694-700.

[37] Su, L.;Jo, E.; Manthiram, A. Protection of Cobalt-Free LiNiO2 from Degradation with Localized Saturated Electrolytes in Lithium-Metal Batteries. *ACS Energy Letters* **2022**, *7*, 2165-2172.

[38] Yang, H.;Guo, C.;Chen, J.;Naveed, A.;Yang, J.;Nuli, Y.; Wang, J. An Intrinsic Flame-Retardant Organic Electrolyte for Safe Lithium-Sulfur Batteries. *Angew. Chem. Int. Ed.* **2019**, *58*, 791-795.

[39] Xue, Y.;Wang, Y.;Zhang, H.;Kong, W.;Zhou, Y.;Kang, B.;Huang, Z.; Xiang, H. Molecular design of mono-fluorinated ether-based electrolyte for all-climate lithium-ion batteries and lithium-metal batteries. *Angew. Chem. Int. Ed.* **2025**, *64*, e202414201.

[40] Joho, F.; Novák, P. SNIFTIRS investigation of the oxidative decomposition of organic-carbonate-based electrolytes for lithium-ion cells. *Electrochim. Acta* **2000**, *45*, 3589-3599.

[41] Zhang, H.;Zeng, Z.;Ma, F.;Wang, X.;Wu, Y.;Liu, M.;He, R.;Cheng, S.; Xie, J. Juggling Formation of HF and LiF to Reduce Crossover Effects in Carbonate Electrolyte with Fluorinated Cosolvents for High-Voltage Lithium Metal Batteries. *Adv. Funct. Mater.* **2023**, *33*, 2212000.

[42] Zhou, J.;Ma, B.;Wang, Q.;Su, L.;Yang, K.;Song, X.;Dou, X.;Wang, M.;Shangguan, X.; Li, F. Anion-regulated weakly solvation sulfolane-based electrolyte towards high-voltage lithium metal batteries. *Chem. Eng. J.* **2025**, *504*, 158857.

[43] Zhao, D.;Cui, G.;Liu, W.; Wu, Z. Nonflammable localized high-concentration phosphazene electrolytes for enhanced safety and interfacial stability in high-voltage lithium metal batteries. *Electrochim. Acta* **2025**, *537*, 146884.

[44] Qin, M.;Zeng, Z.;Wu, Q.;Liu, X.;Liu, Q.;Cheng, S.; Xie, J. 1,3,5-Trifluorobenzene endorsed EC-free electrolyte for high-voltage and wide-temperature lithium-ion batteries. *Journal of Energy Chemistry* **2023**, *85*, 49-57.

[45] Jiang, Z.;Mo, J.;Li, C.;Li, H.;Zhang, Q.;Zeng, Z.;Xie, J.; Li, Y. Anion-Regulated Weakly Solvating Electrolytes for High-Voltage Lithium Metal Batteries. *ENERGY & ENVIRONMENTAL MATERIALS* **2023**, *6*, e12440.

[46] Wang, J.;Yamada, Y.;Sodeyama, K.;Chiang, C. H.;Tateyama, Y.; Yamada, A. Superconcentrated electrolytes for a high-voltage lithium-ion battery. *Nat. Commun.* **2016**, *7*, 12032.

[47] Yoon, E.;Lee, J.;Byun, S.;Kim, D.; Yoon, T. Passivation Failure of Al Current Collector in LiPF6-Based Electrolytes for Lithium-Ion Batteries. *Adv. Funct. Mater.* **2022**, *32*, 2200026.

[48] Li, C.;Wu, S.;Qiu, Y.; Lu, D. Phosphorus-Containing C12H27O4P as Functional Electrolyte Additives for High-Voltage LiNi0.5Mn1.5O4/Graphite Li-Ion Batteries with Excellent Electrochemical Performance. *Advanced Materials Interfaces* **2021**, *8*, 2001588.

[49] Nguyen, M. T.;Pham, H. Q.;Berrocal, J. A.;Gunkel, I.; Steiner, U. An electrolyte additive for the improved high voltage performance of LiNi0.5Mn1.5O4 (LNMO) cathodes in Li-ion batteries. *J. Mater. Chem. A* **2023**, *11*, 7670-7678.

[50] Han, Y.;Jiang, Y.-S.;Yu, F.-D.;Deng, L.;Ke, W.;Zhang, S.-J.;Que, L.-F.;Wu, B.;Ding, F.;Zhao, L.; Wang, Z.-B. Addressing Mn Dissolution in High-Voltage LiNi0.5Mn1.5O4 Cathodes via Interface Phase Modulation. *Adv. Funct. Mater.* **2022**, *32*, 2207285.

[51] Cheng, H.;Ma, Z.;Kumar, P.;Liang, H.;Cao, Z.;Xie, H.;Cavallo, L.;Kim, H.;Li, Q.;Sun, Y.-K.; Ming, J. High Voltage Electrolyte Design Mediated by Advanced Solvation Chemistry Toward High Energy Density and Fast Charging Lithium-Ion Batteries. *Adv. Energy Mater.* **2024**, *14*, 2304321.

Electronic Supplementary Material

High-voltage stability of ethylene carbonate (EC) and an EC-based electrolyte for 5 V-class $LiNi_{0.5}Mn_{1.5}O_4$ batteries

Tingyu Zhao[1], Hexiang Lan[1], Jiajia Zhu[1], Weiming Wang[1], Aiping Jin[1]✉, Jun Xiong[1], Junjun Peng[1], Ming Li[2], and Linghui Yu[1,3]✉

[1] *School of Chemistry and Chemical Engineering, Wuhan Textile University, 1 Sunshine Avenue, Jiangxia, Wuhan 430200, China*
[2] *School of Resources and Environment, Wuhan Textile University, 1 Sunshine Avenue, Jiangxia, Wuhan 430200, China*
[3] *Hubei Key Laboratory for Clean Recycling and Resource Utilization of Waste Fibers, Wuhan Textile University, 1 Sunshine Avenue, Jiangxia, Wuhan 430200, China*

✉Address correspondence to Aiping Jin, jinaiping2000@163.com; Linghui Yu, lhyu@wtu.edu.cn

Supporting information to https://doi.org/10.26599/NR.2026.94909069

Experimental

Materials

$LiPF_6$ (99.90%) and EC (99.95%) were received from Suzhou Duoduo Chemical Technology Co., Ltd. 1,1,2,2-tetrafluoroethyl-2,2,3,3-tetrafluoropropyl ether (TTE, ≥99.5%) was purchased from Shanghai Aladdin Biochemical Technology Co., Ltd. N-methyl-2-pyrrolidone (NMP, ≥99.0%) were purchased from Sinopharm Chemical Reagent Co., Ltd. All the chemicals were used as received except that TTE was dried using molecular sieves (4 Å) for more than one week before use. $LiNi_{0.5}Mn_{1.5}O_4$ (LNMO) and Super P Li were purchased from MTI Corporation, Shenzhen. Polyvinylidene (PVDF) fluoride used was Kynar HSV900.

Electrolytes

1.0 M $LiPF_6$ in EC/DEC/EMC (1/1/1 by volume) with 1.0 wt% VC (LB-240) was obtained from Suzhou Duoduo Chemical Technology Co., Ltd. The EC/TTE electrolyte (0.5 M $LiPF_6$ in EC/TTE) was prepared by adding 1 mmol $LiPF_6$ into the mixture of EC (1 mL) and TTE (1 mL). The control electrolyte (0.5 M $LiPF_6$, LB-240/TTE) was prepared by mixing LB-240 (1 mL) and TTE (1 mL). Electrolyte preparation was conducted in an argon-filled glovebox.

Electrodes

The graphite (Gr) and $LiFePO_4$ (LFP) were purchased from MTI Corporation, Shenzhen. The Gr electrode is composed of 93.2 wt% Gr, 2.5 wt% conductive carbon black, 2.5 wt% styrene-butadiene rubber (SBR), and 1.8 wt% sodium carboxymethyl cellulose. The areal loading of Gr was between 5.6 mg cm^{-2} and 6.4 mg cm^{-2}. The LFP electrode contained 95.4 wt% LFP, 2.5 wt% conductive carbon black, 2 wt% PVDF, 0.1 wt% XOANONS® LD1128 dispersant. The areal loading of LFP was between 12.0 mg cm^{-2} and 12.7 mg cm^{-2}. The current collectors for the Gr and LFP electrodes are copper foil and aluminum foil, respectively. The LNMO electrodes were prepared by dispersing/dissolving LNMO, Super P Li, and PVDF into NMP to form a uniform slurry first. The slurry was cast onto an aluminum foil and then dried in an oven at 80 °C overnight. The LNMO electrode used for half cell (Li/LNMO) tests was composed of 80 wt% LNMO, 10 wt% Super P Li, and 10 wt% PVDF. The areal loading of LNMO was between 3.5 – 3.8 mg cm^{-2}. For the full cell (Gr/LNMO) tests, the LNMO electrode consisted of 90 wt% LNMO, 5 wt% Super P Li, and 5 wt% PVDF, with an areal loading of 11.6 mg cm^{-2} – 12.3 mg cm^{-2} for the LNMO.

Electrochemical measurements

The electrodes were assembled into 2032-type coin cells in an argon-filled glovebox for evaluation. The separator was a glass fiber membrane (ϕ16 mm, pore size 0.8 μm, Shanghai Xinya). Each cell contained 120 μL of electrolyte. Cyclic voltammetry (CV)/linear sweep voltammetry (LSV) and electrochemical impedance spectroscopy (EIS) measurements were conducted on a Biologic SP-200. The scanning rate for the CV/LSV was 5 mV s^{-1}. For the EIS measurements, the frequency range used was 4 MHz to 100 mHz and the amplitude was 10 mV. iR correction used the ohmic resistance of the corresponding cell determined by the EIS measurements. Battery cycling tests were performed using a Neware battery tester. Li/LFP cells used for high-voltage tests were charged to 7 V at a current density of 15 mA g^{-1}. Li/LFP cells used for floating charge tests were first charged to 5 V at a current density of 15 mA g^{-1} and then kept at 5 V until the current density reduced to 1 mA g^{-1}. Li/LNMO cells were cycled in the voltage range of 3.5 V – 4.95 V at a current density of 15 mA g^{-1} in the initial three cycles and 200 mA g^{-1} in the following cycles. For Li/Gr cells, the cycling voltage was set between 0.005 V and 3 V, with a current density of 15 mA g^{-1} for the first two cycles and 100 mA g^{-1} for the following cycles. Gr/LNMO cells were cycled at a current of 15 mA g^{-1} in the voltage range of 3.5 V – 4.85 V for the initial three cycles. In the subsequent cycles, the cells were cycled at a current of 100 mA g^{-1} in the voltage range of 3.5 V – 5 V. The current density and specific capacity of Li/LFP cells were calculated based on the mass of LFP. The current density and specific capacity of Li/LNMO and Gr/LNMO cells were calculated based on the mass of LNMO. The current density and specific capacity of Li/Gr cells were calculated based on the mass of Gr. All the electrochemical measurements were conducted at room temperature.

Material characterizations

Raman spectroscopy was performed on a LabRAM Odyssey Raman spectrometer (Horiba) with a laser excitation of 532 nm. For the nickel and manganese dissolution measurements, the electrolytes of Li/LNMO cells after 103 cycles were collected and the nickel and manganese concentrations were determined using inductively coupled plasma optical emission spectrometry (ICP-OES, Agilent 5800). Transmission electron microscopy (TEM, JOEL JEM-2100F) and X-ray photoelectron spectroscopy (XPS, Thermo SCIENTIFIC ESCALAB Xi+) were used to analyze the LNMO after the 10^{th} charge to 4.95 V in Li/LNMO cells. The cells were disassembled and the LNMO was collected, rinsed with dimethyl carbonate, and dried in an argon-filled glove box. TEM images were acquired at an electron accelerating voltage of 200 kV. XPS experiments were conducted under a base pressure below 10^{-9} mBar. Monochromatic Al Kα radiation (1486.68 eV) was used as the X-ray source. The XPS samples were loaded into the instrument via a glovebox without any air exposure. Charge referencing was performed using the adventitious carbon C-C peak at 284.8 eV.

Theoretical calculations

All Density Functional Theory (DFT) calculations were performed using the Vienna Ab initio Simulation Package (VASP)[1]. The projector augmented wave (PAW)[2] pseudopotential with the PBE[3] generalized gradient approximation (GGA) exchange correlation function was utilized in the computations. All energetics of metal oxides were calculated using the DFT with the Hubbard-U framework (DFT+U) to account for strongly localized d-electrons for Mn, Ni. The Hubbard-U correction terms were at U_{eff} (Mn) = 4.5 eV, U_{eff} (Ni) = 5.96 eV as obtained via linear response theory. The cutoff energy of the plane waves basis set was 500 eV and a Monkhorst-Pack mesh of 2×2×1 was used in K-sampling. All structures were spin polarized and all atoms were fully relaxed with the energy convergence tolerance of 10^{-5} eV per atom, and the final force on each atom was < 0.05 eV $Å^{-1}$.

The adsorption energy of reaction intermediates can be computed using the following equation:

$$\Delta E = E_{\mathrm{ads-H}} - E_{\mathrm{ads}} \quad (1)$$

Where $E_{\mathrm{ads-H}}$ and E_{ads} are the free energy of the model that adsorbs the corresponding molecules, respectively, ads = (*TTE, *EC, *DEC, *EMC, *VC) and ads-H represent the model of ads dehydrogenation.

References

[1] G. Kresse, J.Furthmüller, *Phys. Rev. B* **1996**, *54*, 11169.

[2] P. E. Blöchl, *Phys. Rev. B* **1994**, *50*, 17953

[3] J. P. Perdew, K. Burke, M. Ernzerhof, *Phys. Rev. Lett.* 1996, 77, 3865.

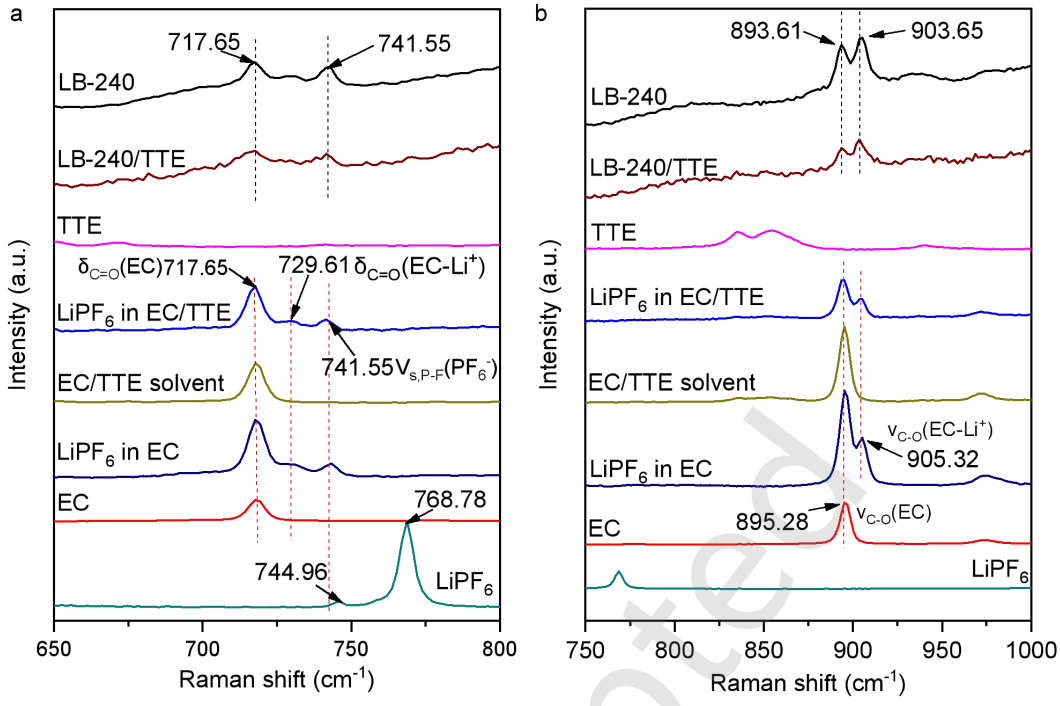

Figure S1. Raman spectra of $LiPF_6$, TTE, solvents, and electrolytes. (a) 650 cm^{-1} – 800 cm^{-1}, and (b) 750 cm^{-1} – 1000 cm^{-1}. The volume ratio of EC and TTE is 1 : 1 in the EC/TTE solvent. A typical $LiPF_6$/EC ($LiPF_6$ in EC) was prepared by dissolving 0.5 mmol of $LiPF_6$ into 0.5 mL of EC. The LB-240/TTE electrolyte and the EC/TTE electrolyte ($LiPF_6$ in EC/TTE) exhibit peak positions identical to those of their respective original electrolytes without TTE, indicating the addition of TTE does not affect the solvation structure. In the EC/TTE electrolyte, only a fraction of EC coordinates with Li^+; the majority stays as free molecules, as evidenced by the free EC peaks (717.65 cm^{-1} and 895.28 cm^{-1}) being far more intense than the coordinated EC–Li^+ peaks (729.61 cm^{-1} and 905.32 cm^{-1}).

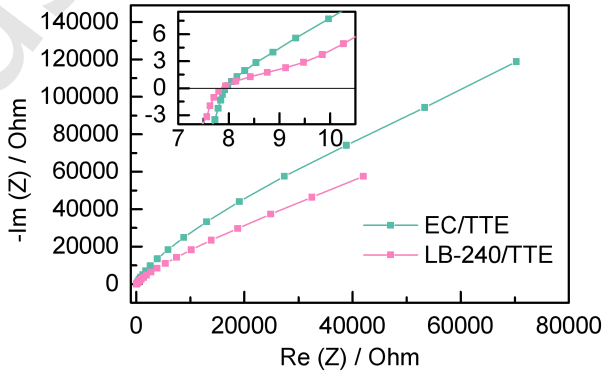

Figure S2. Nyquist plots of Li/Al cells used for iR correction in Figure 1a

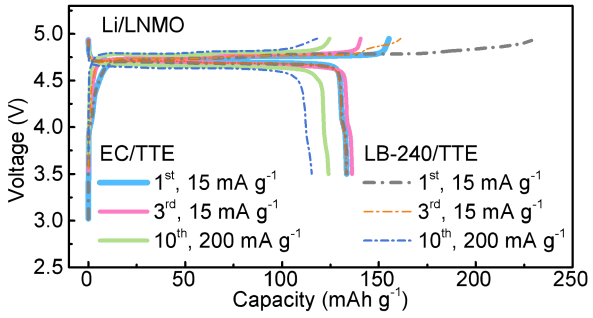

Figure S3. Charge/discharge voltage profiles of Li/LNMO cells

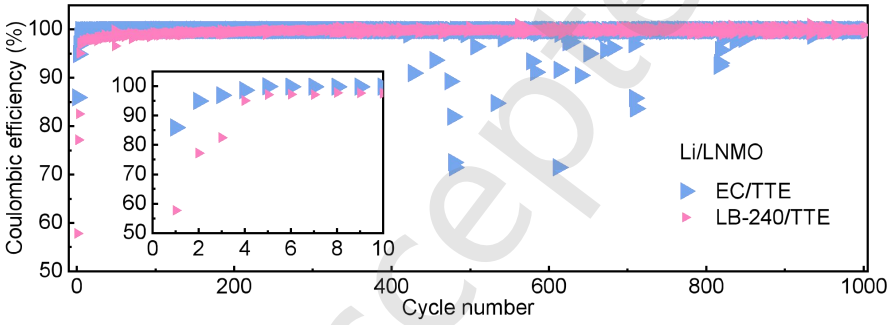

Figure S4. Full range CEs of Li/LNMO. Inset showing the CEs of initial ten cycles

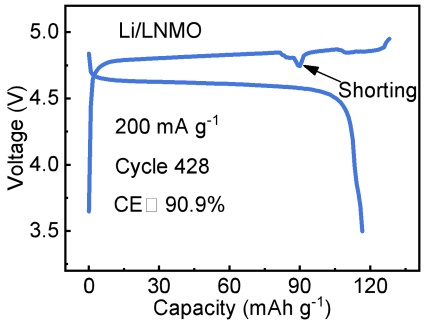

Figure S5. Example of a shorting voltage profile

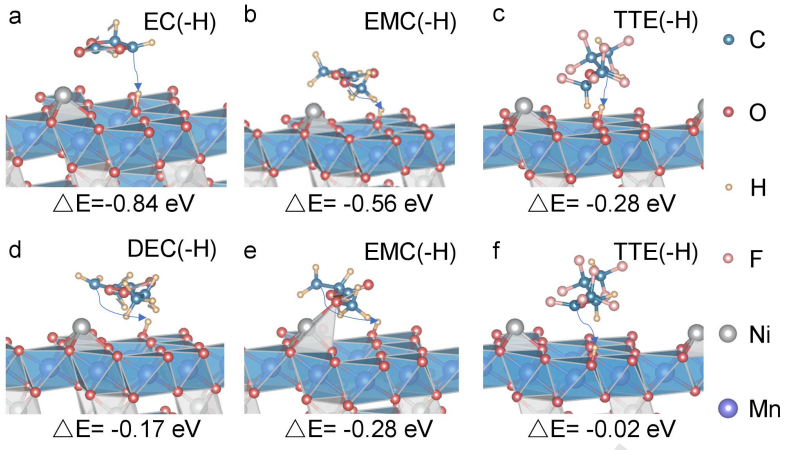

Figure S6. Reactivity of EC, DEC, EMC, VC, and TTE at the fully charged delithiated LNMO ($Ni_{0.5}Mn_{1.5}O_4$) surface (Fd3m, (111)) from DFT+U calculations. More calculation results can be found in Figure 2

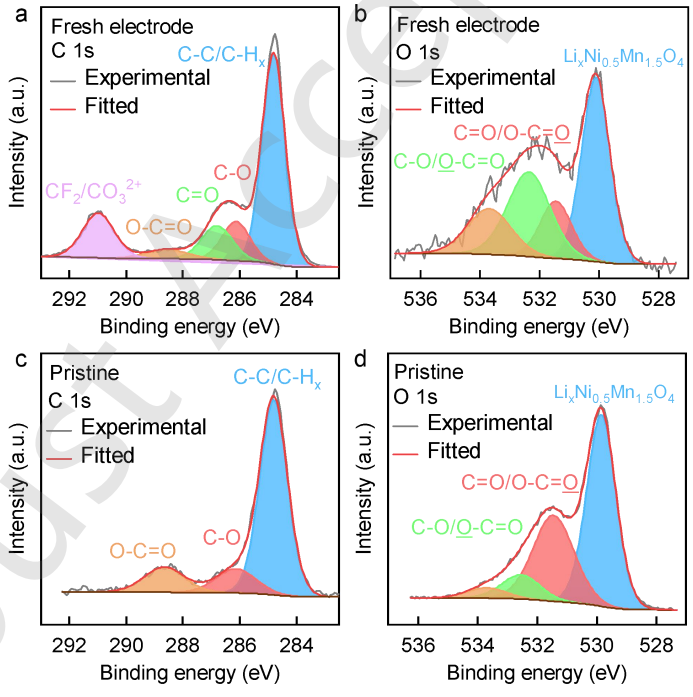

Figure S7. XPS of pristine LNMO and fresh LNMO electrode

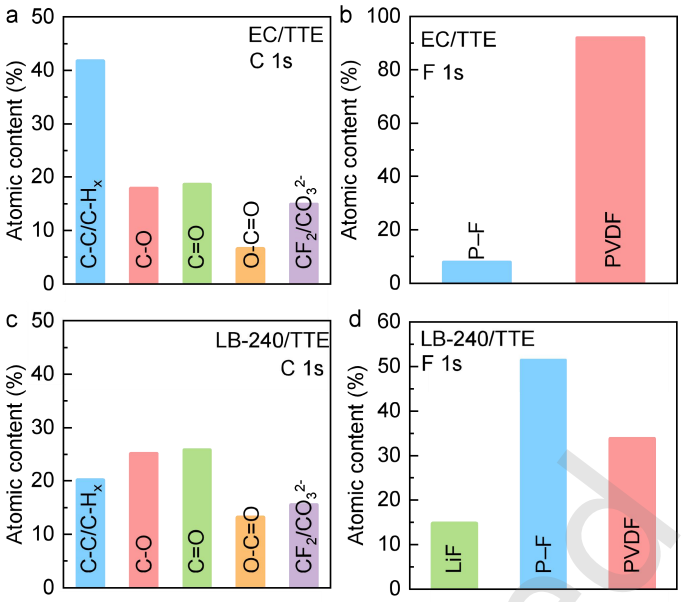

Figure S8. Relative XPS contents of the LNMO electrodes charged to 4.95 V vs. Li^+/Li (10^{th} charge). (a) C-containing species cycled in the EC/TTE electrolyte, (b) F-containing species cycled in the EC/TTE electrolyte, (c) C-containing species cycled in the LB-240/TTE electrolyte, and (d) F-containing species cycled in the LB-240/TTE electrolyte

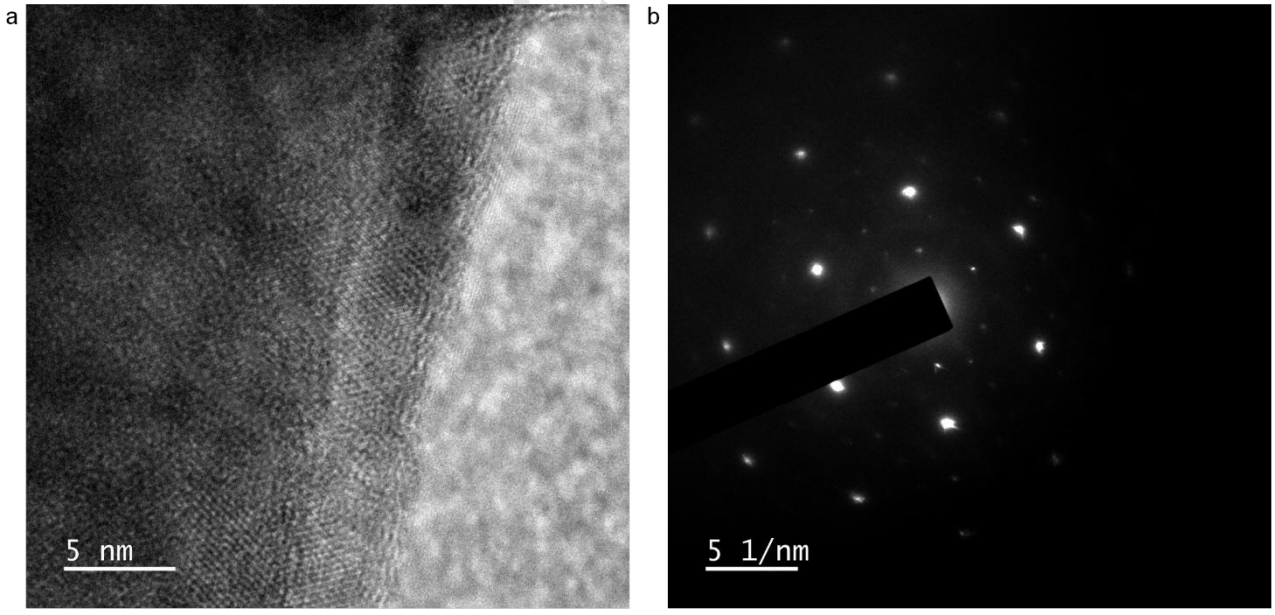

Figure S9. TEM analysis of pristine LNMO. (a) TEM image, and (b) SAED pattern

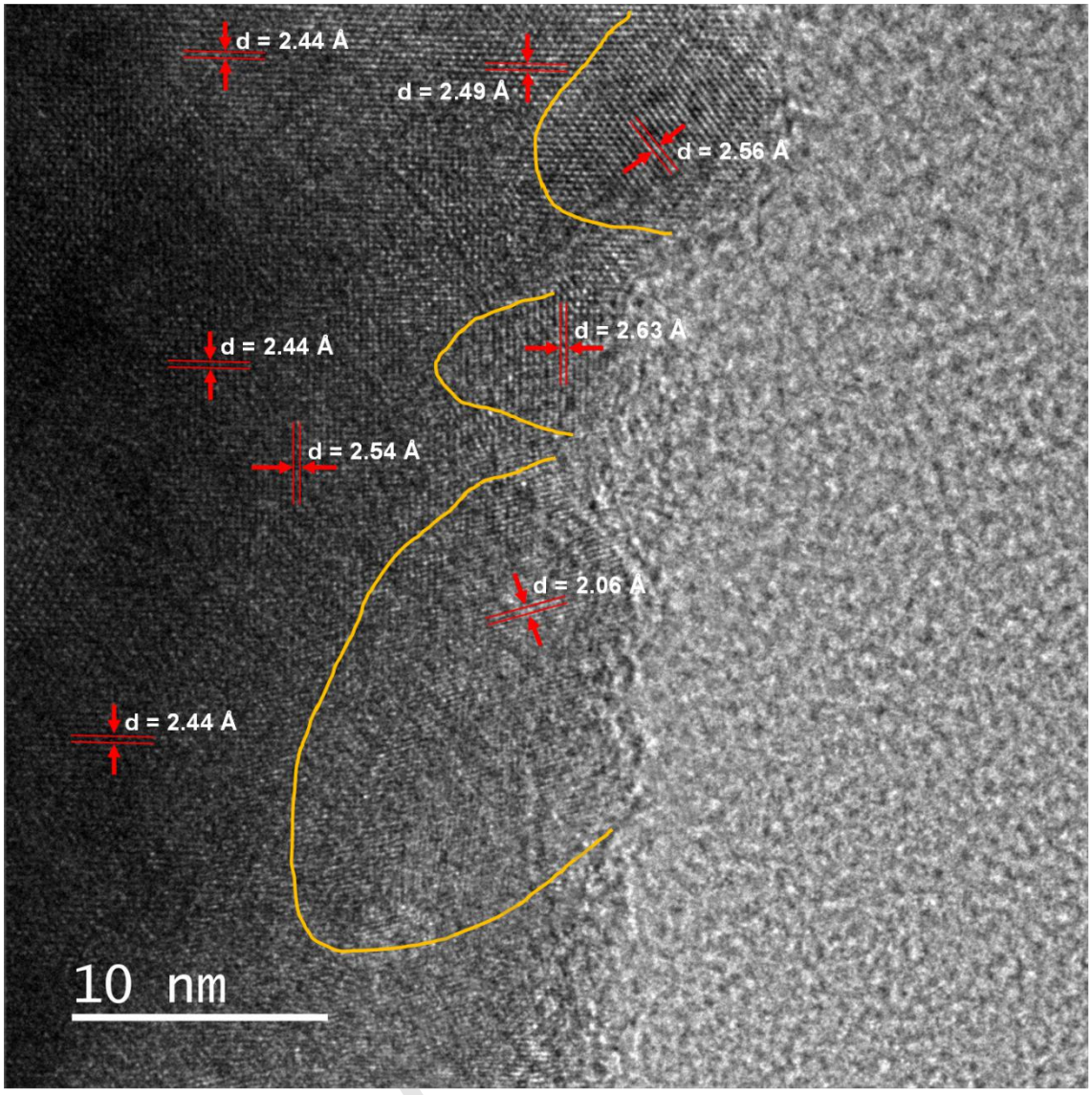

Figure S10. TEM image of the LNMO charged to 4.95 V vs. Li^+/Li (10^{th} charge) in the EC/TTE electrolyte. This figure shows an enlarged view of Figure 4d for clarity.

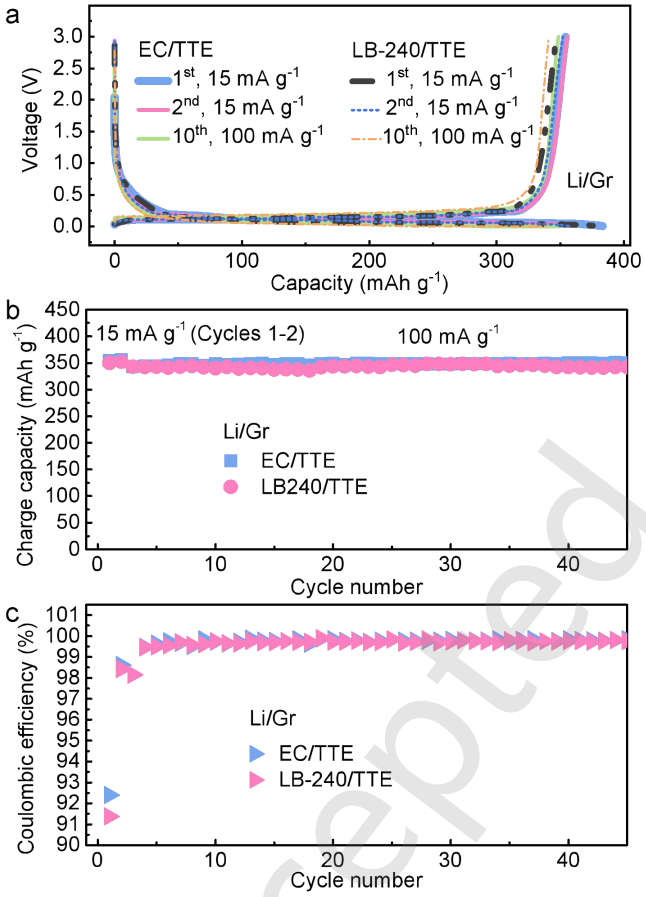

Figure S11. Properties of Li/Gr cells in the EC/TTE and LB-240/TTE electrolytes. (a) Charge/discharge voltage profiles; (b) cyclability; and (c) CEs

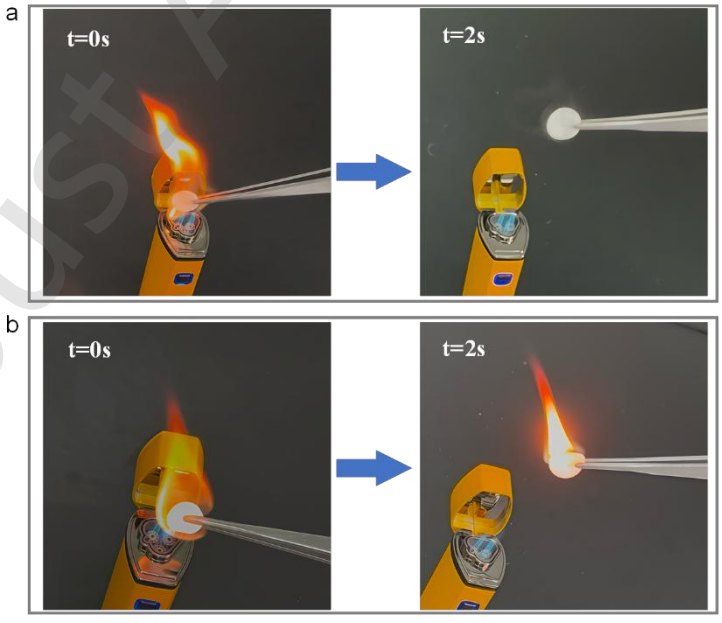

Figure S12. Flammability tests showing the non-flammability of EC/TTE (a) and the high flammability of LB-240/TTE (b)

Table S1. XPS binding energy and relative atomic ratio of the LNMO electrodes charged to 4.95 V vs. Li^+/Li in two electrolytes

			Cycled in the EC/TTE electrolyte	Cycled in the LB-240/TTE electrolyte	Fresh electrode	Pristine LNMO
Peak binding energy (eV)/relative atomic ratio (%)	C 1s	C-C/C-H_x	284.80/41.80	284.80/20.23	284.80/55.23	284.80/73.29
		C-O	285.94/17.95	285.95/25.12	286.12/12.35	286.14/12.99
		C=O	286.83/18.68	287.02/25.89	286.80/11.90	-
		O-C=O	288.90/6.60	288.97/13.21	288.57/4.48	288.66/13.93
		CF_2/CO_3^{2+}	290.54/14.96	290.64/15.54	290.98/16.04	-
	F1s	LiF	-	685.30/14.79	-	-
		P-O	686.26/7.99	686.95/51.40	-	-
		PVDF	687.78/92.01	688.07/33.81	-	-
	O1s	Oxide ($Li_xNi_{0.5}Mn_{1.5}O_4$)	529.99/9.88	-	530.10/41.37	529.84/53.70
		C=O/O-C=<u>O</u>	531.67/19.62	531.45/4.85	531.44/14.31	531.45/33.60
		C-O/<u>O</u>-C=O	532.62/34.26	52.82/47.09	532.35/28.47	532.55/8.80
		To be assigned	534.94/36.24	534.21/48.05	533.68/15.84	533.69/3.89